ORIGINAL ARTICLE

Impact of the interface on the fatigue life of steel-based explosively welded heterostructured plates

Szymon Derda[1] · Aleksander Karolczuk[1] · Grzegorz Robak[1] · Mariusz Prażmowski[1] · Henryk Paul[2] ·
Tadeusz Łagoda[1] · Munish Kumar Gupta[1,3]

Abstract

Melted zones, microcracks, shear bands, and elastic incompatibility of explosively welded materials are features that may initialize cracks at the interface and reduce fatigue strength. This study aims to determine the effect of interfacial defect-like structures on the fatigue strength of explosively welded corrosion-resistant plates. Cyclic axial loading was applied to seven distinct layer-by-layer compositions of Ti Gr 1, Zr 700 alloys, and carbon steels. The interfacial wave height as a metric of potential fatigue life influencing factors along with measured strain amplitude was applied as the input quantities for the Machine Learning based model, i.e. the Gaussian process for regression (GPR). This is a novel and successful application of GPR to estimate the effect of interfacial wave height on the fatigue life of explosively welded plates. For the first time, the effect of the interface feature on fatigue life was estimated quantitatively. The Digital Image Correlation technique was applied to measure the field of cyclic strain for the purpose of verifying if a single strain amplitude is representative of a heterostructured plate. It was found that interfacial wave height is an important feature and its increase by 100 μm reduces the fatigue life of analysed plates by 36%. Additionally, to validate the applicability of explosively welded plates to engineering structures under cyclic loading, the experimental fatigue lives were compared with the design curve of the American Society of Mechanical Engineers (ASME) code.

Keywords Layerwise-heterostructured plates · Fatigue life · Explosive welding · ASME design curve · Digital image correlation · Gaussian process for regression

1 Introduction

The evolution of biological materials has optimised their structures to intricate composites [1]. This has inspired material scientists to design high-performance materials with layerwise architectures to fulfil the increasing industrial demands [2]. The composition of homogeneous layers with intensive variations in their physical properties results in a heterostructured material [3] that offers unique properties applicable in different industrial fields. Layers made of reactive metals (e.g. titanium and zirconium) with excellent corrosion resistance in various environments [4] bonded to

✉ Aleksander Karolczuk
 a.karolczuk@po.edu.pl

 Szymon Derda
 s.derda@po.edu.pl

 Grzegorz Robak
 g.robak@po.edu.pl

 Mariusz Prażmowski
 m.prazmowski@po.edu.pl

 Henryk Paul
 h.paul@imim.pl

 Tadeusz Łagoda
 t.lagoda@po.edu.pl

 Munish Kumar Gupta
 munishguptanit@gmail.com

1 Opole University of Technology, ul. Mikołajczyka 5,
   45-271 Opole, Poland

2 Institute of Metallurgy and Materials Science, Polish
   Academy of Sciences, ul. W. Reymonta 25, 30-059 Kraków,
   Poland

3 Department of Mechanical Engineering, Graphic Era
   (Deemed to Be University), Dehradun, India

materials with superior mechanical properties (steels) can provide the expected synergistic effect. Owing to its exclusively high corrosion resistance, low absorption capacity for thermal neutrons, and great biocompatibility, Zr is principally applied in the nuclear [5], chemical [6], and biomedical industries [7]. The corrosion resistance of titanium is complementary to that of zirconium [4] and its alloys are applied in energy [8] and aerospace [9] industries as well as chemical and hydrometallurgical processes [10]. Since zirconium and titanium are more expensive than alternatives like stainless steel, their application is restricted. The application of stainless steel is also limited owing to its insufficient working temperature and corrosion resistance [11]. The application of layerwise-heterostructured metallic plates with a relatively thin layer of zirconium or titanium alloy provides a solution to this problem. According to Banker [12], such composites are cost-effective for heavy-wall vessels and heat exchangers. These engineering structures may be subjected to cyclic stresses that arise from periodic changes in the operating pressure and temperature, vibration, fluctuations in the flow of fluids or solids, and the periodic variability of external loads [13]. Fatigue loading could lead to failure, for example, fatigue cracks were found in the plates of heat exchangers made of Ti Gr 1 alloy [14] and 316L stainless steel [15]. Fatigue failure of big heat exchangers has been identified as a serious issue in the industry by a number of studies [16].

The fabrication of layerwise-heterostructured metallic plates composed of materials with different physical and chemical properties (i.e. dissimilar metals, e.g. titanium–steel, zirconium–steel, [17]) poses technological problems [18]. Explosive welding is a technology capable of joining dissimilar metals and has the unique ability to produce large plates [19]. Xie et al. [20] presented the mechanical and structural properties of Ti/steel bimetallic sheets with an area of 20 m^2 fabricated via explosive welding. Zhang et al. [21] successfully joined duplex stainless steel to X65 pipe steel plates with an area of 12 m^2. In this impact welding process, the chemical energy of the explosives is transformed into the kinetic energy of the flyer plate (Fig. 1), which collides with the base plate [17]. The line of

collision propagates along the base plate from the ignition spot at high velocities (2000–3000 m/s). The high pressure and temperature localised in the vicinity of the impact area provide the conditions for bond formation. The bonding mechanism is still the subject of many studies [22, 23]. It is commonly accepted that (i) during a collision, the thin layers of joint materials are transformed into a fluid phase forming a jet effect (Fig. 1) that cleans the joint surfaces and enables the creation of a metallurgical bond; (ii) severe plastic deformation occurs near the interface; (iii) a typical interface has a periodical wavy geometry; (iv) melted zones can be found in the form of thin layers or pockets; and (v) intermetallic phases and microcracks can be induced in the melted zones. The intensity of the aforementioned features depends on the applied welding parameters and properties of the joint materials [24]. Recently, Zhou et al. [25] discovered a relationship between the ultimate tensile strength of bimetallic specimens (Ti/Steel) and the interfacial wave height. It was observed that the highest periodic wave exhibited the highest ultimate tensile strength. Chen et al. [26] observed cracks and voids at the wavy interface of Ti/stainless steel that weakened the bonding strength. Furthermore, adiabatic shear bands (ASBs) have been observed in titanium [27] and zirconium [28] layers near the interface. However, the observed severe plastic deformation results in grain refinement and strain hardening of the steel and titanium layers [29] adhering to the interface, which may increase the ultimate tensile and fatigue strengths of the composite.

The melted zones, microcracks, brittle intermetallic phases, ASBs, and wavy interfaces of materials with rapid changes in mechanical properties (elastic incompatibility) are stress-raising features that can initiate cracks and decrease the fatigue strengths of explosively welded metallic plates. However, the standardised mechanical testing of multilayer metallic plates for pressure vessels (ASTM B898: Specification for a reactive and refractory metal clad plate) includes only bond shear strength testing and ductility bond testing under monotonic loading. Monotonic tensile testing, microhardness measurements, and Charpy impact testing commonly support research on explosively welded multilayer metallic plates. Mechanical testing under fatigue

Fig. 1 Explosive welding scheme with a micrograph of Ti/steel interface
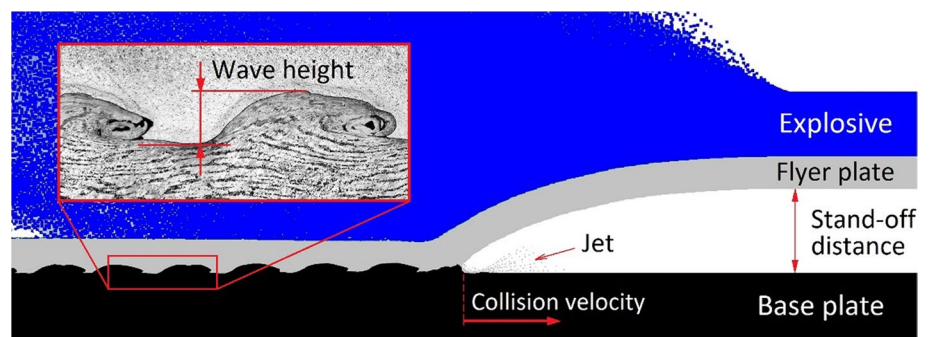
loading is more complex and requires a larger number of specimens—increasing the cost of the experiment. The prohibitive costs of reactive and refractory materials, fatigue testing, and explosive welding itself have limited the published studies on the fatigue properties of explosively fabricated corrosion-resistant materials.

Jiang et al. [30] analysed the fatigue crack growth in a stainless steel/mild steel bimetallic notched plate under cyclic four-point bending. They concluded that the interface induced a shielding effect for the crack growth owing to the plasticity mismatch between materials. The shielding effect of the interface was also observed by Zhou et al. [31] in notched three-layer specimens composed of Zr 702 alloy, TA2 titanium alloy, and Q345R steel. Ostroushko and Mazancova [32] studied the influence of heat treatment (annealing at 600 °C) on the fatigue life of a Cr18Ni10 stainless steel/titanium bimetallic plate under cyclic three-point bending with a stress ratio of R = 0.1 (with tensile stress variations in the titanium layer). It was found that the fatigue lives of specimens after the heat treatment increased by a factor ranging from 1.1 to 2.0 at high cyclic fatigue ($N > 10^5$ cycles) but decreased by a factor ranging from 1.2 to 2.0 at low cyclic fatigue. Wachowski et al. [33] also investigated the influence of heat treatment (annealing at 600 °C) on the fatigue life of a bimetallic specimen composed of 316L stainless steel and a Ti Gr 1 alloy. The specimens were also tested under cyclic three-point bending with a stress ratio of R = 0.1 (inducing only tensile stress variations in the titanium layer). However, in this case, the heat treatment decreased the fatigue life by a fixed factor of 1.6. In addition, Wachowski et al. [34] applied the cyclic three-point bending to an S355 steel/Ti Gr 1 alloy bimetallic specimen before and after heat treatment (annealing at 600 °C). The results revealed a significant decrease in fatigue life by a factor of 3.0 due to heat treatment.

In the aforementioned testing under three-point bending with tensile stress variations in titanium, the fatigue cracks initiated on the outer surface of the titanium layer and then propagated into the interface. Kurek et al. [35] applied fully reversed cyclic bending (R = − 1) to an S355 steel/Ti Gr 1 bimetallic specimen with an equal layer thickness before and after heat treatment (annealing at 600 °C). It was found that the heat treatment significantly decreased the fatigue life of the bimetallic specimen by a factor of 6.0. After heat treatment, fatigue cracks initiated in the outer surface of the titanium layer and then propagated into the interface. However, the majority of fatigue cracks in the specimen initiated in the outer layer of the steel without heat treatment. Karolczuk et al. [36] analysed the fatigue behaviour of an S355 steel/Ti Gr 1 bimetallic plate after heat treatment (annealing at 600 °C) subjected to cyclic fully reversed (R = − 1) push–pull loading with the force applied in the direction parallel to the interface. It was found that only 20% of the

fatigue failures were initiated at the interface. The remaining 80% of failures were initiated at the outer surface of the S355 steel layer. The specimen with the smallest interfacial wave height showed the longest fatigue life. Karolczuk et al. [28, 37] tested two- and three-layer plates using a Zr 700 alloy flyer plate and a base plate of different steel types. In the case of the three-layer composite, the interlayer was composed of Ti Gr 1 or Zr 700 alloy. The plates were not subjected to heat treatment. Fully reversed cyclic push–pull loading was applied parallel to the interface. It was found that the melted zones at the interface with the steel layer were preferential sites for fatigue crack initiation. However, these cracks did not lead to the failure of the composites in most cases. Under uniaxial cyclic loading with the tensile static component (R = 0), the cyclic creep was found as the dominant failure mechanism in Ta/Cu/steel multilayer plates [38].

Under bending fatigue loading, the highest stress alternation occurs on the outer surface of the plate. Consequently, cracks do not initiate at the interface. The observed detrimental effect of annealing on the lifetime of steel/titanium bimetallic plates is attributed to the redistribution of the residual stress and reduction in the strain hardening effect in the titanium alloy (manifested by the hardness reduction). The heat treatment increases the number of brittle phases [39]; however, these phases are located in the melted zones, and thus, their influence on fatigue crack initiation under cyclic bending is insignificant. The existence of intermetallic phases can have a more pronounced detrimental effect under push–pull loading. Push–pull loading has a more severe effect than cyclic bending on the fatigue strength of multilayer plates because the interface is not 'hidden' from the load bearing, and the existing interfacial defects provide conditions for fatigue crack initiation. The interface morphology with its stress-raising features can be considered as the weakest fatigue link in an explosively welded multilayer plate. However, grain refinement, strain hardening near the interface, and compressive residual stresses can prevent crack initiation and development.

The question arises: Do the stress-rising features in the interface of explosively welded metals reduce the fatigue life of multilayer plates?

The objective of the current research is to estimate the effect of interface features on the fatigue life of steel-based explosively welded plates. To fulfil the defined aim, we applied the Machine Learning (ML) technique to capture the hidden pattern in the fatigue data of several explosively welded metallic plates. The Gaussian Process for Regression (GPR) [40] was selected among various ML techniques due to (i) its ability to work on small datasets [41], (ii) its unique ability to provide prediction uncertainty, and (iii) small number of parameters to be identified if compared with other ML techniques. The GPR is a data-driven approach that enables

the discovery of an unknown and highly non-linear interaction between multidimensional inputs and one-dimensional output.

Six experimental data sets of multilayer plates with zirconium and/or titanium layers bonded to steel layers and subjected to cyclic push–pull loading were collected from previously published studies. The data sets were enlarged by new experimental tests on a Ti Gr 1/Cu/ SA516 Gr 70 layerwise plate. The resulting sets comprising data from seven multilayer plates enabled for the first time to quantitatively estimate the effect of the interfacial feature on fatigue life owing to the novel application of the GPR. The interfacial wave height as a metric of potential fatigue life influencing factors along with measured strain amplitude was applied as the input quantities (predictors) for the GPR model. To verify if the single strain amplitude is representative of a heterostructured plate, the Digital Image Correlation (DIC) technique was applied to measure the field of cyclic strain. Additionally, to validate the applicability of explosively welded plates to engineering structures under cyclic loading, the experimental fatigue lives were compared with the design curve of the ASME code [42].

2 Materials and methods

The fatigue data necessary to replicate the analysis along with detected crack initiation sites were reposited in [48], including the photos of the fatigue fracture surfaces and geometry of specimens.

2.1 Materials

In the present research, experimental results of seven multilayer plates, each with a corrosion-resistant layer (flyer plate), constructed of Zr 700 alloy or Ti Gr 1 alloy, were analysed. The results for the six plates have already been published in [28, 36, 43]. However, the current research included additional data on micrographs with fatigue cracks and strain–life curves. These data were supplemented by a

new experimental test conducted on a Ti Gr 1–Cu–SA516 Gr 60 three-layer plate. ZTW Explomet was the exclusive manufacturer of multilayer plates (Opole, Poland).

Table 1 displays the mechanical properties of the constituent materials that constitute their basic features with respect to the welding process (elongation at break, a minimum of 20% is required for explosive welding), generation of residual stress (mismatch between the thermal expansion coefficients), stress concentration (mismatch between Young's moduli), generation of additional stress components (mismatch between Poisson's ratios), and fatigue strength (the yield and ultimate tensile strengths are indicators related to the fatigue strength). A parallel explosive welding system (Fig. 1) was applied to all plates with the standoff distances and detonation velocities presented in Table 2. The detonation velocities were measured using a Kontinitro Explomet-Fo-2000 measuring system. The designations in Table 2 assigned to the multilayer plates are short versions of the welded plates consistently used in the subsequent sections of this article. One two-layer plate, i.e. Ti–S355, was heat treated at 600 °C for 90 min.

The integrity of the welded plates was assessed via ultrasonic examination. The results of the microscopy measurements with respect to the interface wave height H and length n at several locations are listed in Table 3 in the form of the mean ± standard deviation. The melted area at the interface with the steel layer was also measured and divided by the length of the welded line, resulting in the equivalent melted thickness (*EMT*) [43]. The wave height and *EMT* values were analyzed (see SubSects. 3.1 and 3.3) in terms of their relation to the fatigue cracking that initiated at the interface. The representative melted areas with shrinkage cracks and ASBs are depicted in Fig. 2.

X-ray microcomputed tomography (Phoenix V|tome|x S240) revealed an irregular interface wave formation (Fig. 3) on the Zr–10CrMo9 interface. The interfacial waves vary in height and length, and the wave crests do not form continuous curves. This typical tomography shows that the bond formation has a strong local characteristic. The observed discontinuities in the interfacial wave

Table 1 Basic mechanical properties of constituent materials for explosive welding at ambient temperature

Material	Young's modulus, GPa	Poisson's ratio	Yield strength, MPa	Ultimate strength, MPa	Elongation at break, %	Thermal expansion coefficient, 10^{-6}/ °C
Zr 700	101	0.38	216 (R_{p02})	269	35	7.2
Ti Gr 1	109	0.37	251 (R_{p02})	325	46	8.5
Cu (M1E)	128	0.34	103 (R_{p02})	219	50	16.7
S355J2 + N	204	0.30	417 (R_{eH})	590	29	12.0
SA516 Gr 60	193	0.29	268 (R_{p02})	391	41	12.0
SA516 Gr 70	200	0.29	371 (R_{eH})	532	31	12.0
10CrMo9-10	212	0.28	447 (R_{eH})	568	26	11.5

Table 2 Parameters of the explosion welding process

Multilayer plate	Flyer	t, mm	Interlayer	t, mm	Base	t, mm	Detonation velocity, m/s	Standoff distance δ, mm
Zr–Gr70	Zr 700	3.5	–	–	Gr 70	20	2500	3
Zr–10CrMo9	Zr 700	3.5	–	–	10CrMo9-10	18	2500	9
Ti–S355	Ti Gr 1	6	–	–	S355	40	*	*
Zr–Zr–Gr60	Zr 700	10	Zr 700	3.5	Gr 60	25	3000	6 + 25 (flyer δ Zr δ Gr 60)
Ti–Cu–Gr70	Ti Gr 1	10	Cu	1.5	Gr 70	20	*	*
Zr–Ti–Gr60(1)	Zr 700	10	Ti Gr 1	2.0	SA516 Gr 60	14	2500	10 (flyer δ Ti/Gr 60)
Zr–Ti–Gr60(2)	Zr 700	10	Ti Gr 1	2.0	SA516 Gr 60	14	2500	15 (flyer δ Ti/Gr 60)

t layer thickness, *confidential data

Table 3 Wave height, length, and *EMT*

| Structure	Plate	Interface	Wave height H, μm	Wavelength n, μm	*EMT*, μm
Two-layer	Zr–Gr70	Zr/Gr 70	122 ± 28	577 ± 129	12.6
	Zr–10CrMo9	Zr/10CrMo9	276 ± 73	1384 ± 166	13.5
	Ti–S355	Ti/S355	132 ± 43	627 ± 154	2.9
Three-layer	Zr–Zr–Gr60	Zr/Zr	207 ± 27	783 ± 104	–
		Zr/Gr 60	343 ± 67	1442 ± 173	73.3
	Ti–Cu–Gr70	Ti/Cu	17 ± 8	244 ± 69	–
		Cu/Gr 70	216 ± 76	744 ± 197	3.7
	Zr–Ti–Gr60(1)	Zr/Ti	207 ± 38	1012 ± 146	–
		Ti/Gr 60	71 ± 27	464 ± 149	3.2
	Zr–Ti–Gr60(2)	Zr/Ti	236 ± 27	1325 ± 195	–
		Ti/Gr 60	67 ± 23	405 ± 114	5.1

Fig. 2 Cracks in the melted zones at the bond interfaces in selected multilayer plates observed before fatigue testing
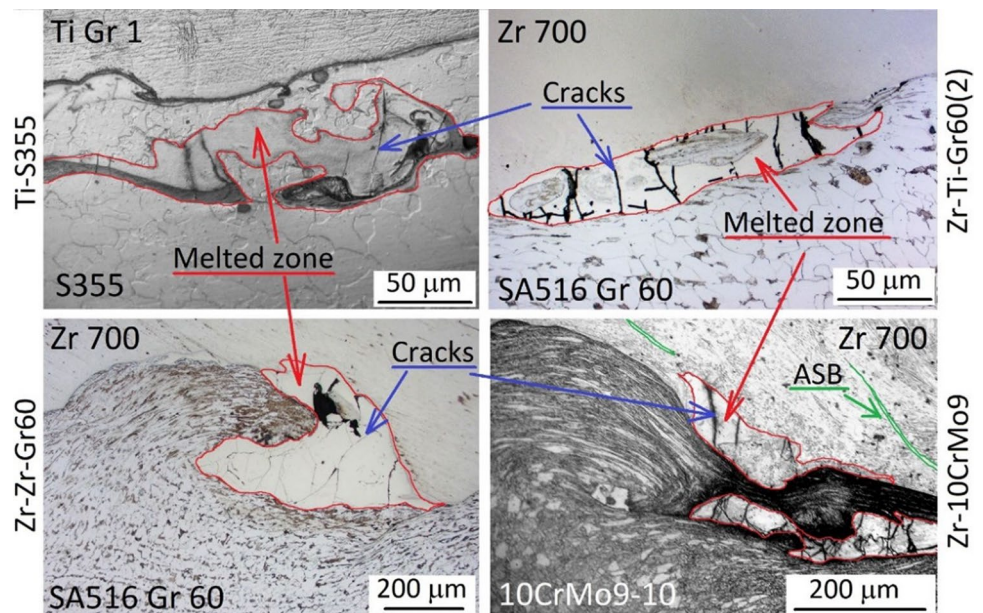
formation under fatigue loading can increase the stress field inhomogeneity and fatigue life scatter in the case of failures initiated at the interface.

The interface microstructure of a steel layer with a Zr or Ti layer has been extensively investigated in many studies. It is commonly recognised that such an interface is

Fig. 3 X-ray microcomputed tomography of Zr–10CrMo9 interface
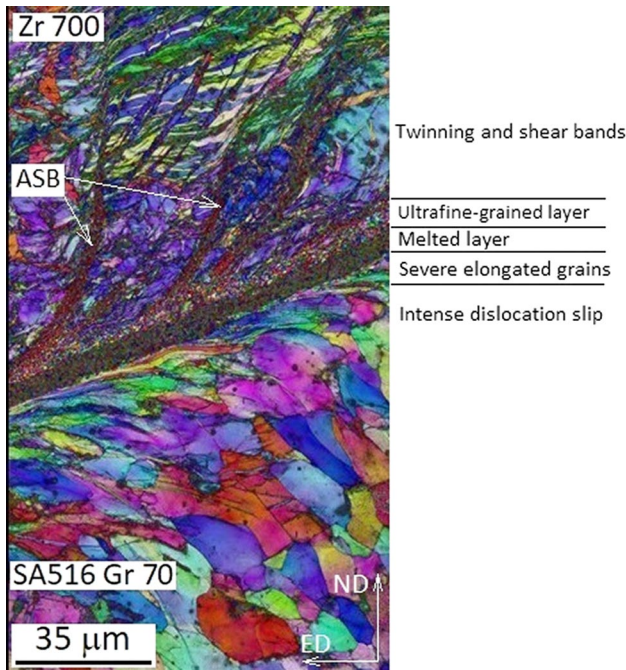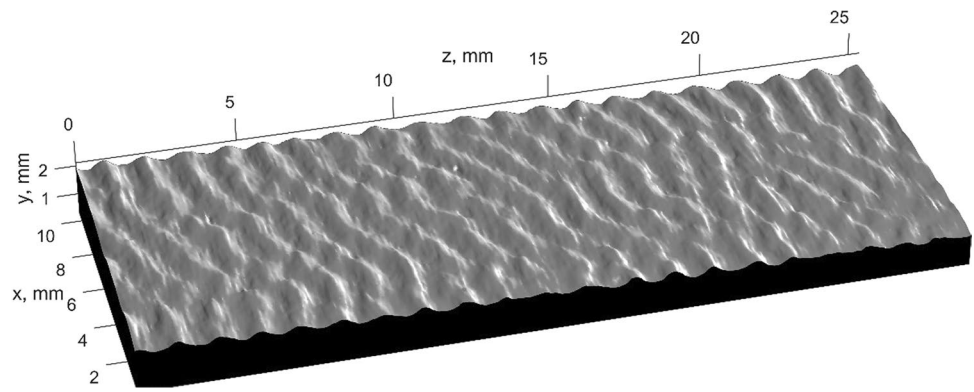
Fig. 4 ASBs in Zr 700 layer and elongated grains in SA516 Gr 70 steel adhering to the melted layer revealed by an inverse pole figure map (*ED* explosive direction, *ND* normal direction). Scanning electron microscopy coupled with an electron backscatter diffraction setup with a step size of 100 nm was employed for the analysis

Table 4 Thicknesses (t_1, t_2, and t_3) of layers and widths (w) of specimens in the gauge section

Plate t_1–t_2–t_3	t_1, mm	t_2, mm	t_3, mm	w, mm	Number of tested specimens
Zr–Gr70	3.40	–	5.40	11.90	4
Zr–10CrMo9	3.44	–	5.53	12.01	6
Ti–S355	3.05	–	5.92	9.73	12
Zr–Zr–Gr60	$t_1 + t_2 = 7.92$		4.16	8.95	7
Ti–Cu–Gr70	5.21	1.43	5.30	9.02	5
Zr–Ti–Gr60(1)	5.26	1.95	4.78	8.70	9
Zr–Ti–Gr60(2)	5.43	1.94	4.64	8.98	7

2.2 Fatigue testing

The multilayer plates manufactured for industrial applications were designed by the supplier (ZTW Explomet) for industrial applications. The initial total thicknesses of the plates were up to 46 mm (Ti–S355). The original plate thickness was reduced to adapt the cross-sectional area of the specimen to the applied capacity of the hydraulic fatigue machine (± 50 kN). The geometry of the plane specimens differed owing to the different number of layers; however, their thickness ratios were retained when possible (separately for the two- and three-layer plates). The thicknesses of the layers and widths of all specimens were measured using digital microscopy. The mean values of the measurements are displayed in Table 4. The geometries of the specimens, fatigue data (to reproduce the results), and photographs of the fracture surfaces were reposited in [48]. The specimens for the six plates were cut along the detonation wave direction, except for the Ti–S355 plate, whose specimen axis and propagation direction of the detonation wave intersected at an angle of 57°. The specimens were subjected to fully reversed force-controlled cyclic loading at room temperature (~20 °C). Failure was defined as complete specimen separation, and the number of loading cycles (sinusoidal

characterised by a pronounced hierarchical microstructure with an extremely fine-grained structure near the interface [44]. ASBs [45] are found in Zr and Ti layers adhering to a thin (1–10 μm) melted layer that includes amorphous phases and nanograins of intermetallic phases [46]. A typical microstructure is represented by the analysed Zr700–Gr70 interface displayed in Fig. 4. With respect to fatigue strength, the ASBs are localised damage bands along which fatigue cracks can develop [47]. The ultrafine and elongated thin grains in the steel layer can form obstacles for fatigue crack growth in the plane normal to the interface.

signal) to failure was counted based on this definition. The strain signals were recorded using a mechanical extensometer mounted on a steel layer with a gauge length of 25 mm.

2.3 Gaussian process regression (GPR)

The GPR a non-parametric Bayesian probabilistic method for uncovering multidimensional patterns in datasets. Its applicability to the fatigue life prediction of homogenous materials has been demonstrated in several studies [49, 50]. The GPR technique is accessible through several statistical packages (e.g. Matlab 2021b, Statistics and Machine Learning Toolbox were applied here) and its theoretical background is thoroughly described in [40]. However, the basic concept of the GPR is required to understand the result analysis. The GPR assumes that the observed output y_i for a given multidimensional input point x_i is normally distributed and the collection of $i = 1 \ldots n$ distributions can be described by a multivariate Gaussian distribution. The multivariate (joint) distribution is defined by the vector of means and the covariance matrix. The zero means in the GPR are usually assumed [40]. The principal concept of the GPR is the assumption of similarities between the outputs that are reflected by the distance r (radius) between input points. To apply this concept, the components of the covariance matrix in GPR are the functions of r (i.e. covariance function or kernel). By conditioning (Bayesian inference) the multivariate Gaussian distribution on the observed training data, the median outputs, and its variance for unseen input points were derived [40]. In constructing the GPR model, the covariance function and predictors must first be selected.

2.3.1 Selected input features – predictors

Strain amplitude ε_a (measured at half-life in the steel layer) and interfacial wave height H (Table 3) were used as predictors (model inputs). The GPR assumes a normal distribution of the output $y(x)$ for each input multidimensional point x (i.e. $x = [\varepsilon_a, H]$ in the present study). To fulfil this requirement, the 10-base logarithm of fatigue life was applied. It was concluded that the stress and force amplitudes were not appropriate for describing the testing conditions because the dataset consists of multilayer plates varying in layer arrangement and content. The hardness was also considered a potential predictor but due to its significant inhomogeneous distribution along the layers, this feature was rejected.

2.3.2 Kernel selection

In regular GPR application, the stationary radial-based kernels are applied in which the distance r between the input points x_p, x_q is defined as

$$r = \sqrt{(x_p - x_q)^T M (x_p - x_q)}, \tag{1}$$

where $M = \text{diag}(l_i)^{-2}$ is a diagonal matrix of scale parameters $l_i = l_1, \ldots, l_d$ (d is the number of predictors). In fatigue life prediction problems presented in [49, 50], the exponential (EX) or squared exponential (SE) covariance functions were effectively applied. The application EX kernel in the current research resulted in significant data overfitting reflected by peculiar variations of predicted fatigue lives. The predicted fatigue life must be decreasing function of the applied strain amplitude. If this physic rule is not simulated by the applied GPR model, the kernel should be rejected. The fatigue lives obtained by the GPR with the SE kernel satisfied the physic rule and thus only this kernel is described here. The SE kernel takes the following form

$$k(x_p, x_q) = \sigma_k^2 \exp\left(-\frac{1}{2}r^2\right) \tag{2}$$

where σ_k^2 is the variance of the (noise-free) signal. The applied GPR assumed that the observed outputs contain the noise ϵ of the normal distribution with a standard deviation σ_y, i.e., $y = f(x) + \epsilon \sim \mathcal{N}(0, \sigma_y^2)$. This assumption is included in the GPR by increasing the diagonal components in the covariance function.

The model parameters, i.e. two scale parameters l_{ε_a}, l_H, standard deviations σ_k, and σ_y were found by maximizing log marginal likelihood by applying a quasi-Newton optimizer with the trust-region method (Matlab 2021b, Statistics and Machine Learning Toolbox).

2.3.3 Interpretation method

An intuitive way to inspect the results of GPR is the application of the Partial Dependence Plot (PDP) [51] and Individual Condition Expectation (ICE) plots [52]. The basic motivation was to observe the character of changes in predictions depending on the selected predictor. The PDP computes the n model responses $\hat{f}(x_s, x_{i,-s})$ in the function of the analysed predictor x_s for observing other predictors $x_{i,-s}$ (excluding–s predictor) and the individual outputs are averaged

$$\hat{f}_S(x_s) = \frac{1}{n} \sum_{i=1}^{n} \hat{f}(x_s, x_{i,-s}) \tag{3}$$

where n denotes the number of training points. The averaged process may hide interesting model behaviour and thus the ICE was developed with the potential to reveal heterogenous effects. The ICE is a disaggregation of PDP, i.e. the individual curves estimated by $\hat{f}(x_s, x_{i,-s})$ that display a functional relationship between response and a predictor for individual observation.

2.4 Digital image correlation (DIC)

Displacement measurement and strain calculation were conducted with the use of a commercial DIC setup provided by Dantec Dynamics (2D measurement with the application of DSM 15450 Camera, 5.0 Mpx, CMOS, 77 fps, Sensor Size: 2/3" and Schneider-Kreuznach Lens, 50 mm focal length). A full description of the correlation method can be found in [53]. In the present study, the method was implemented to inspect the inhomogeneity of the strain distribution in the multilayer specimen. To improve the contrast between the background and speckles, the surface of the specimen was covered with white paint, then tiny black dots were introduced with the airbrush. In the presented case the speckle size allowed to perform correlation with the facet size equal to 17 by 17 pixels with a resolution of 6.2 μm/px. To increase the spatial resolution a grid spacing was set to 13 pixels resulting in a 1/4 overlap. Data acquisition was performed automatically based on the force signal at the peak value of the force sine wave provided by the fatigue machine controller.

3 Results and discussion

3.1 Fatigue initiation sites and paths

All fatigue fracture surfaces were analysed using optical microscopy to detect the crack initiation sites. The percentage of failures initiating at the interfaces was calculated for each multilayer plate and compared with the interfacial wave height (Fig. 5a) and equivalent melted thickness (*EMT*) (Fig. 5b). All specimens (100%) from three multilayer plates, i.e. $Zr-10CrMo9$, $Zr-Zr-Gr60$, and $Ti-Cu-Gr70$, exhibited fatigue failures initiating at the interface with the steel. This corresponded to the interfacial wave height recorded

for the same plates (Fig. 5a). The results did not reveal any relationship between the *EMT* and the percentage of failures initiating at the interface (Fig. 5b).

The interrupted fatigue tests or final observation revealed that cracks frequently originated at the interface with the steel layer; however, in most cases, they did not lead to the disintegration of the multilayer plate. The fatigue crack that originated at the interface of multilayer plates without heat treatment exhibited similar behaviour. Representative examples of fatigue cracks and fracture surfaces were displayed in Figs. 6 and 7. The cracks initiated in the melted area and spread into the steel layer at an angle in the range of 45°–76° to the interface (Figs. 6 and 7a). On the other side, the crack grew partially along the interface (Figs. 6a and 7b) with the adjacent layer (Ti, Zr or Cu) and then along the ASB in the case of the Ti or Zr layer (Fig. 6b).

For the Ti–S355 plate subjected to heat treatment different crack behaviour was observed. The cracks indicated in Fig. 8a spread along the boundary of the melted zone (red circle in Fig. 8a) and the decarburized and curled steel layer. The cracks branched off at the interface with Ti Gr 1 and spread into the Ti grains.

The explosively welded multilayer heterostructured plates are characterised by a pronounced hierarchical and inhomogeneous microstructure [54]. With respect to fatigue strength, the observed strain hardening and grain refinement at the interface vicinity form beneficial features, but the melted pockets with microcracks and shear bands are the major stress-raising factors with detrimental effects. In homogeneous materials with ultrafine grains, intergranular fatigue cracking was observed in iron [55]. This crack behaviour was not observed in the explosively welded Ti/Zr/steel multilayer materials. All fatigue cracks that initiated at the interface revealed transgranular behaviour.

Two distinct features of the crack length in the plane of the applied maximum nominal shear stress were observed
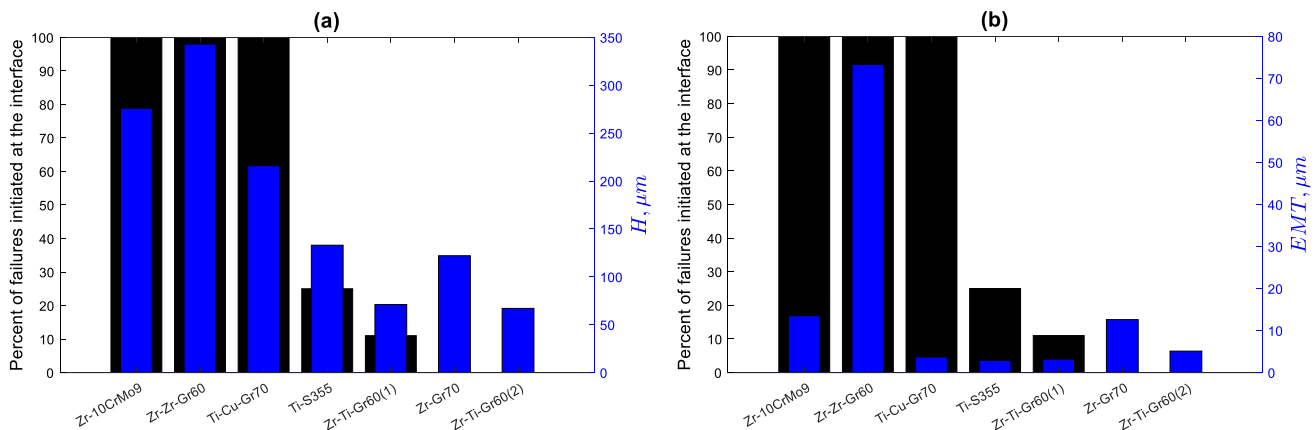

Fig. 5 Percent of specimen failures initiating at the interface compared to the **a** interface wave height *H* and **b** equivalent melted thickness (*EMT*)
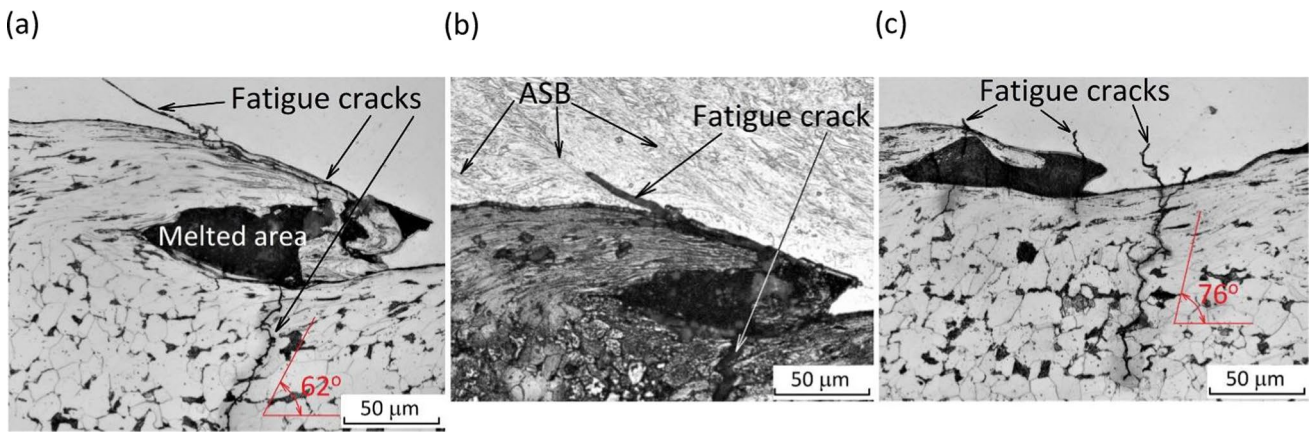
Fig. 6 Fatigue cracks at the Ti Gr 1–Gr60 interface of the Zr–Ti–Gr60(2) plate for the specimen that failed at N = 270 687 cycles
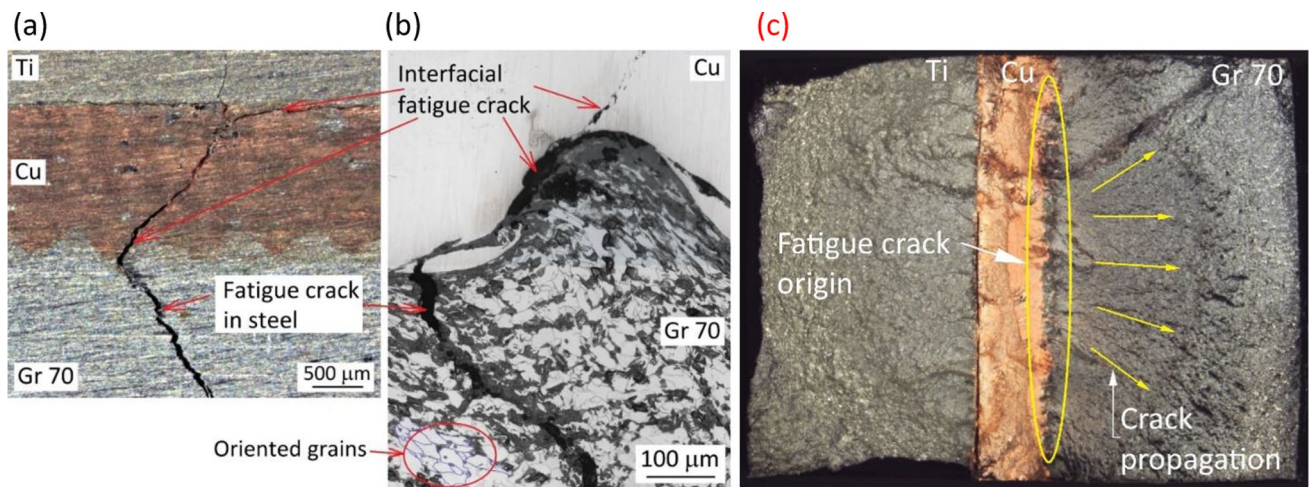

Fig. 7 **a** and **b** Fatigue cracks at the Ti–Cu–Gr70 interface, **c** fatigue fracture surface
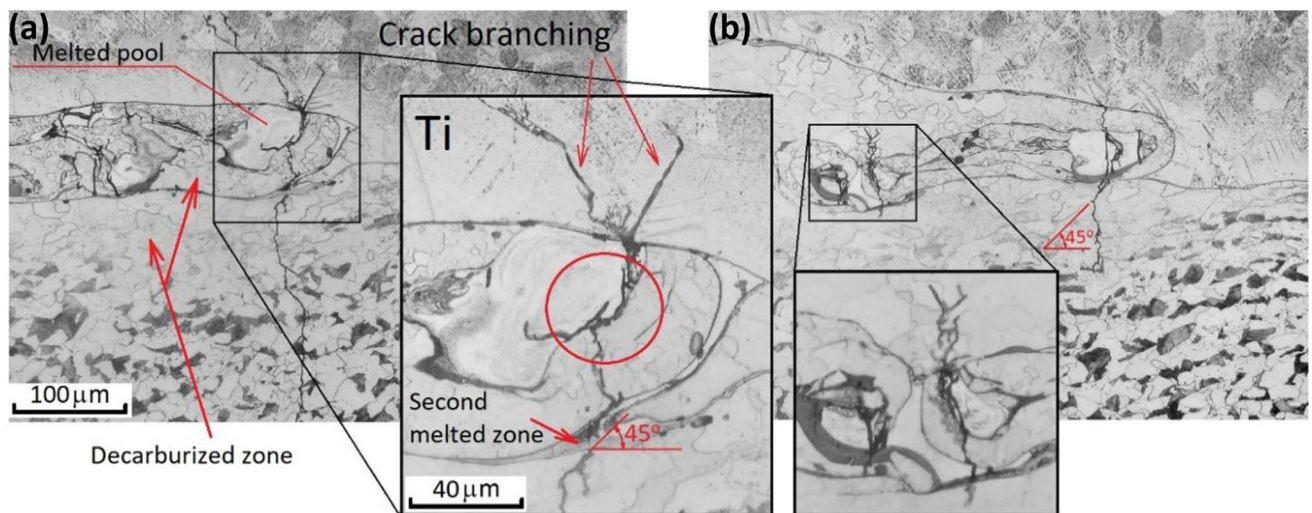

Fig. 8 Fatigue cracks at the interface of Ti Gr 1–S355 plate

in the analysed plates. The Ti–S355 plate specimens subjected to heat treatment revealed a limited number of fatigue cracks initiating at the interface. The heat treatment resulted in a 100 μm thick recrystallised layer adhering to the interface. The cracks found at the interface initiated at the maximum shear plane; however, this fracture stage occupied only a single grain and then propagated along the maximum principal stress plane (Fig. 8). In contrast, the fatigue cracks initiated at the interface in the specimens cut out from the plates without heat treatment extended across several grains in the plane close to the maximum applied shear stress (Fig. 6). The melted pockets at the interface with the steel layer constitute attractive locations for fatigue crack initiation; however, their growth rate depends on the interfacial wave height. For multilayer plates with interfacial wave heights H greater than 200 μm, the cracks initiating at the interface propagated through the steel layer, leading to specimen fracture. For $H < 200$μm, the cracks initiating at the interface propagated at an insufficient rate to lead to specimen fracture in most cases, and the cracks initiating at the steel surface away from the interface prevailed.

3.2 Homogeneity of the cyclic strain field

Zr–Zr–Gr 60 plate was chosen for DIC analysis due to the substantial wave height measured at the Zr–Gr 60 interface and the smallest steel to Zr thickness ratio that should result in the highest non-uniformity of strain distribution (Finite element analysis, FEA). The axial strain fields measured at two fatigue life ratios are presented in Fig. 9.

The observed area of 11.6 mm × 11.0 mm and the applied grid size of 13 px with a resolution of 6.2 *μm*/px resulted in around 20 000 grid points. This high density of grid points revealed multiple fatigue cracks at the interface with the steel layer at 80% of fatigue life (Fig. 9b). However, this high density of grid points resulted in a noisy strain distribution, and the moving average process was required to determine the strain distribution across the layers. The average window size of 0.50 mm × 6 mm ($x \times y$) was applied to receive the standard error below 10% of the mean value. The average axial strain distribution along the x-axis was presented in Fig. 9 by red dot marks along with error bars presenting the 95% confidence intervals of the mean. The linear regression indicates (blue dashed line in Fig. 9) the slope of $3.32 \cdot 10^{-5}$ mm^{-1} at 10% of fatigue life. As a result of this non-uniformity of strain distribution, the difference between
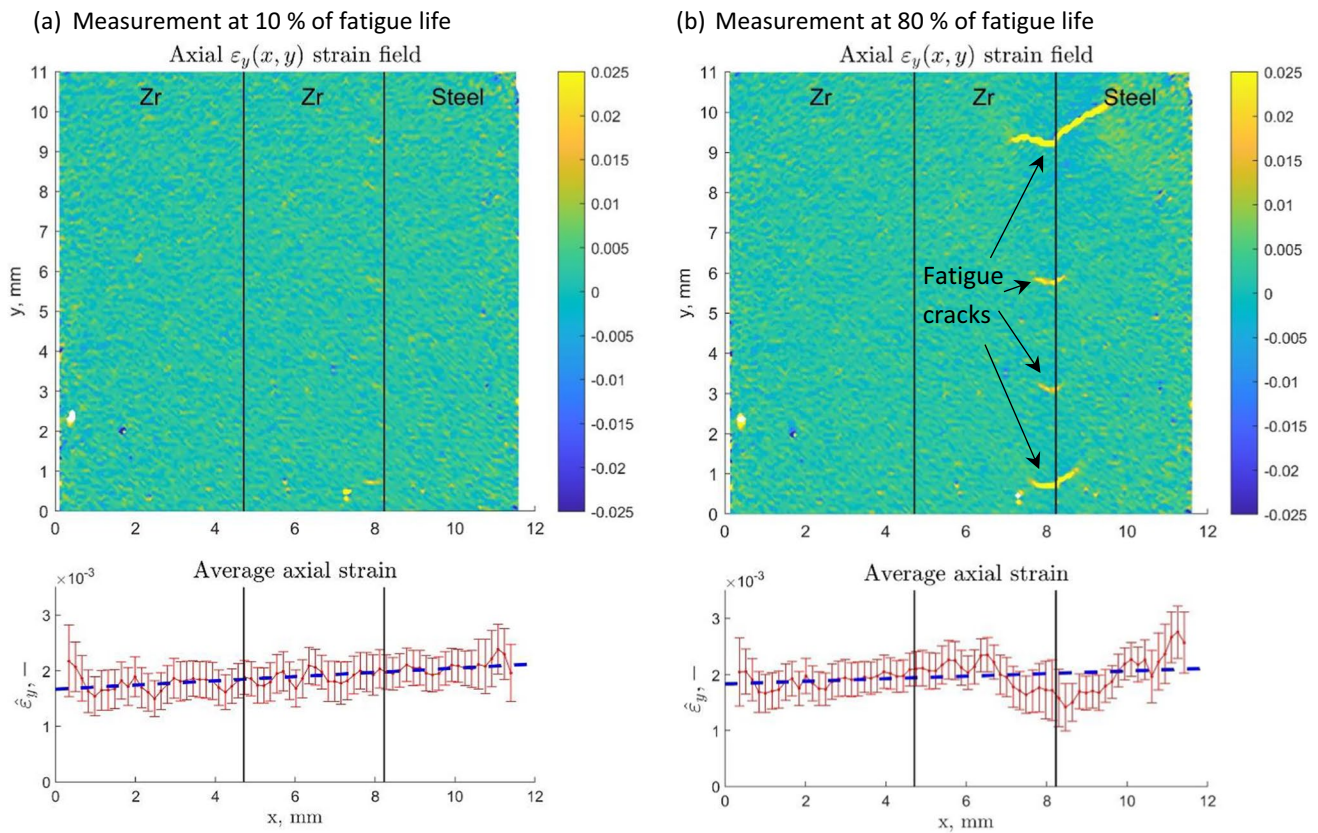
(a) Measurement at 10 % of fatigue life

(b) Measurement at 80 % of fatigue life

Fig. 9 Axial strain distribution measured for force peak at **a** 10% of fatigue life and **b** 80% of fatigue life. Fatigue cracks at the Zr/Steel interface

strain measured at the interface with steel and strain measured by mechanical extensometer (steel surface) is around 6.6% (5% of the difference was estimated by FEA, for other plates it is around 2%). This strain reduction was insignificant for Zr–Zr–Gr60 plate and the cracks were initiated at the interface due to the high interfacial wave height.

3.3 Fatigue life and its relation with the interfacial wave height

The fatigue strain–life results are shown in Fig. 10. The strain amplitudes varied during the cyclic loading and the error bars represent those measured at 0.2 and 0.8 ratios of the total life while the central point denotes the 0.5 ratio. The acquired results were compared to strain-life curves

suggested by the ASME Boiler and Pressure Vessel Code [42], which specifies requirements for the building of nuclear power plant parts. The dashed and solid lines in Fig. 10 represent the ASME mean and design curves for carbon steels, respectively. All experimental points, including their error bars, are located on the conservative side of the design curve with a safety margin higher than 6.6%, i.e. including the detected strain non-uniformity (subSect. 3.2).

The GPR model was able to identify the relationship between fatigue life, strain amplitude, and interfacial wave height (Fig. 11). The estimated prediction intervals are relatively small with a standard deviation σ_y (subSect. 2.3.2) of 0.193. The standard deviation can be recalculated to a 95% fatigue life scatter band as $10^{1.96 \cdot \sigma_y} = 2.39$. This scatter value is acceptable in material fatigue problems [56]
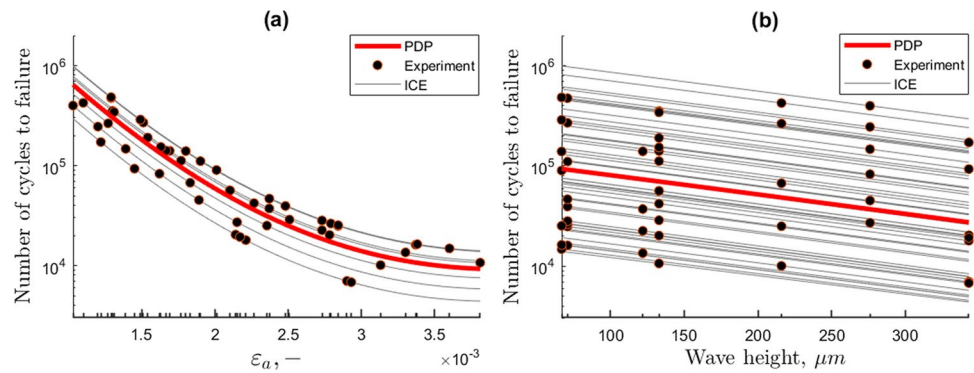

Fig. 10 Strain ε_a amplitudes in relation to the experimental number of cycles to failure
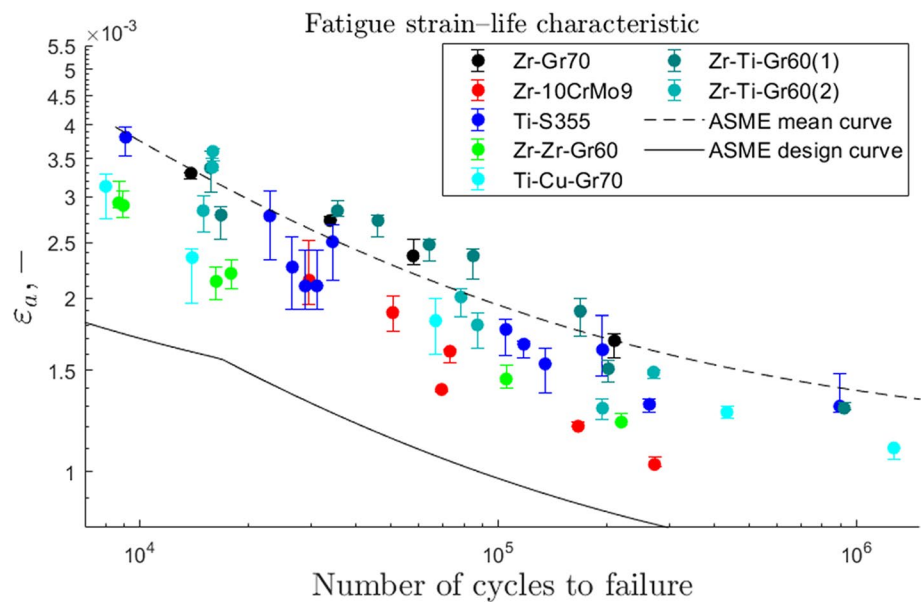
Fig. 11 Gaussian process regression prediction for multilayer plates with 95% confidence intervals
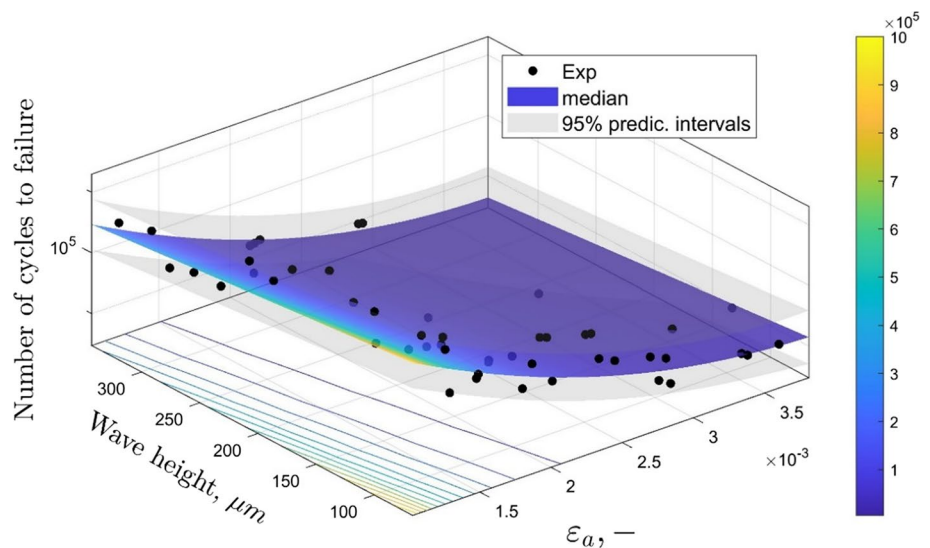
Fig. 12 PDP and ICE plots for each predictor of the GPR model

The influence of strain amplitude and wave height on the fatigue life is reflected by PDP and ICE plots (Fig. 12). The non-linear effect of strain amplitude on lifetime is detected with similar characteristics as presented in Fig. 10 by the ASME mean curve. The effect of interfacial wave height is linear with a homogenous distribution over the strain amplitudes (Fig. 12b). The slope coefficient is defined as $(\log(N + \Delta N) - \log(N))/\Delta H$ is 0.0193. Recalculation led to $10^{-0.0193 \cdot \Delta H} - 1 = \frac{\Delta N}{N}$, thus the increase of the wave height ΔH by 100 μm reduces the fatigue life by 36%.

The strain hardening detected by the increase in hardness intensifies the yield stress [43] of the thin steel layer adhering to the interface. The higher hardness of steel also indicates a higher fatigue strength [57]. The melted pockets with microcracks must be treated as defects with sizes correlating with the interfacial wave height. According to Murakami et al. [58], the fatigue limit σ_w of materials with defects or cracks is related to the Vickers hardness HV of the metal matrix and the square root of the defect area projected onto a plane perpendicular to the applied stress. This explains the observed crack behaviour in the explosively welded plates. The fatigue strength of the steel zone adhering to the interface is increased by strain hardening (hardness increase) but decreased by defect formation. If the defect size reaches the critical length, the fatigue strength of the defective layer is lower than that of the steel layer unaffected by the welding process. The interfacial wave height H is a feature capturing strain hardening and defected structure effects on the fatigue life of analysed composite plates.

- The interfacial wave height is a feature correlating with the fatigue life of the analysed composite plates. The applied Gaussian process for regression identified its effect as linear relation on the log scale of a lifetime. The increase of interfacial wave height by 100 μm decreased fatigue life by 36%.
- The composite plates with corrosion-resistant flyer sheets made of Ti Gr 1 or Zr 700 explosively bonded to carbon steels satisfy the ASME fatigue design curves.
- The brittle melted pockets at the interface with the steel layer are attractive locations for fatigue crack initiation.
- The measured axial strain field for the Zr–Zr–Gr60 composite exhibited a 6.6% higher strain peak for the steel surface than for Zr–Gr60 interface. The DIC measurement of the strain field can be applied to the early detection of fatigue crack initiation.
- Fatigue testing of explosively welded plates at higher temperatures must be conducted to confirm their applicability under different service conditions.

4 Summary and conclusions

To investigate the effect of the interface of explosively welded plates on fatigue life, the Gaussian process for regression was applied to the collected experimental data set. The following conclusions were drawn:

Declarations

by another journal. We have read and understood your journal's policies, and we believe that neither the manuscript nor the study violates any of these.

References

1. Barthelat F, Yin Z, Buehler MJ. Structure and mechanics of interfaces in biological materials. Nat Rev Mater. 2016;1:1–16. https://doi.org/10.1038/natrevmats.2016.7.

2. Liu Z, Meyers MA, Zhang Z, Ritchie RO. Functional gradients and heterogeneities in biological materials: Design principles, functions, and bioinspired applications. Prog Mater Sci. 2017;88:467–98. https://doi.org/10.1016/j.pmatsci.2017.04.013.

3. Zhu Y, Ameyama K, Anderson PM, Beyerlein IJ, Gao H, Kim HS, Lavernia E, Mathaudhu S, Mughrabi H, Ritchie RO, Tsuji N, Zhang X, Wu X. Heterostructured materials: superior properties from hetero-zone interaction. Mater Res Lett. 2021;9:1–31. https://doi.org/10.1080/21663831.2020.1796836.

4. Ning J, Zhang L, Xie M, Yang H-X, Yin X, Zhang J. Microstructure and property inhomogeneity investigations of bonded Zr/Ti/steel trimetallic sheet fabricated by explosive welding. J Alloys Compd. 2017;698:835–51. https://doi.org/10.1016/j.jallcom.2016.12.213.

5. Li MH, Ma M, Liu WC, Yang FQ. Recrystallization behavior of cold-rolled Zr 702. J Nucl Mater. 2013;433:6–9. https://doi.org/10.1016/j.jnucmat.2012.09.022.

6. Igolkin AI. Use of zirconium for mechanization of chemical processes. Chem Pet Eng. 1999;35:111–7. https://doi.org/10.1007/BF02363032.

7. Northwood DO. The development and applications of zirconium alloys. Mater Des. 1985;6:58–70. https://doi.org/10.1016/0261-3069(85)90165-7.

8. Schutz RW, Watkins HB. Recent developments in titanium alloy application in the energy industry. Mater Sci Eng A. 1998;243:305–15. https://doi.org/10.1016/s0921-5093(97)00819-8.

9. Boyer RR. An overview on the use of titanium in the aerospace industry. Mater Sci Eng, A. 1996;213:103–14. https://doi.org/10.1016/0921-5093(96)10233-1.

10. Grauman JS, Say T. TITANIUM for hydrometallurgical extraction equipment. Adv Mater Processes. 2000;157:25.

11. Oberndorfer M, Thayer K, Kästenbauer M. Application limits of stainless steels in the petroleum industry. Mater Corros. 2004;55:174–80. https://doi.org/10.1002/maco.200303781.

12. Banker JG. Explosion cladding: an enabling technology for zirconium in the chemical process industry, ASTM, 2010.

13. Towler G, Sinnott R. Design of pressure vessels, in: Chemical Engineering Design, Butterworth-Heinemann, 2022: pp. 441–495. https://doi.org/10.1016/b978-0-12-821179-3.00014-5.

14. Pelliccione AS, SantAnna R, Siqueira MHS, Ribeiro AF, Ramos JE, Silva OP, Pimentel MF. Failure analysis of a titanium plate heat exchanger – Mechanical fatigue. Eng Fail Anal. 2019;105:1172–88. https://doi.org/10.1016/j.engfailanal.2019.07.059.

15. Martins GSM, da Silva RPPD, Beckedorff L, Monteiro AS, de Paiva KV, Oliveira JLG. Fatigue performance evaluation of plate and shell heat exchangers. Int J Pressure Vessels Piping. 2020;188:104237. https://doi.org/10.1016/j.ijpvp.2020.104237.

16. Ali M, Ul-Hamid A, Alhems LM, Saeed A. Review of common failures in heat exchangers – Part I: Mechanical and elevated temperature failures. Eng Fail Anal. 2020;109:104396. https://doi.org/10.1016/j.engfailanal.2020.104396.

17. Findik F. Recent developments in explosive welding. Mater Des. 2011;32:1081–93. https://doi.org/10.1016/j.matdes.2010.10.017.

18. Fang Y, Jiang X, Mo D, Zhu D, Luo Z. A review on dissimilar metals' welding methods and mechanisms with interlayer. Int J Adv Manuf Technol. 2019;102:2845–63. https://doi.org/10.1007/s00170-019-03353-6.

19. Mendes R, Ribeiro JB, Loureiro A. Effect of explosive characteristics on the explosive welding of stainless steel to carbon steel in cylindrical configuration. Mater Des. 2013;51:182–92. https://doi.org/10.1016/j.matdes.2013.03.069.

20. Xie MX, Zhang LJ, Zhang GF, Zhang JX, Bi ZY, Li PC. Microstructure and mechanical properties of CP-Ti/X65 bimetallic sheets fabricated by explosive welding and hot rolling. Mater Des. 2015;87:181–97. https://doi.org/10.1016/j.matdes.2015.08.021.

21. Zhang LJ, Pei Q, Zhang JX, Bi ZY, Li PC. Study on the microstructure and mechanical properties of explosive welded 2205/X65 bimetallic sheet. Mater Des. 2014;64:462–76. https://doi.org/10.1016/j.matdes.2014.08.013.

22. Wang F, Yang M. Experimental and numerical investigations of platinum foil/titanium plate interfaces prepared by explosive welding. Arch Civil Mech Eng. 2023. https://doi.org/10.1007/s43452-022-00591-6.

23. Solecka M, Mróz S, Petrzak P, Mania I, Szota P, Stefanik A, Garstka T, Paul H. Microstructure-related properties of explosively welded multi-layer Ti/Al composites after rolling and annealing. Arch Civil Mech Eng. 2023. https://doi.org/10.1007/s43452-022-00577-4.

24. Yang M, Ma HH, Shen ZW. Study on explosive welding of Ta2 titanium to Q235 steel using colloid water as a covering for explosives. J Market Res. 2019;8:5572–80. https://doi.org/10.1016/j.jmrt.2019.09.025.

25. Zhou Q, Liu R, Ran C, Fan K, Xie J, Chen P. Effect of microstructure on mechanical properties of titanium-steel explosive welding interface. Mater Sci Eng. 2022;830:142260. https://doi.org/10.1016/J.MSEA.2021.142260.

26. Chen X, Inao D, Li X, Tanaka S, Li K, Hokamoto K. Optimal parameters for the explosive welding of TP 270C pure titanium and SUS 821L1 duplex stainless steel. J Market Res. 2022;19:4771–86. https://doi.org/10.1016/J.JMRT.2022.07.031.

27. Karolczuk A, Paul H, Szulc Z, Kluger K, Najwer M, Kwiatkowski G. Residual stresses in explosively welded plates made of titanium grade 12 and steel with interlayer. J Mater Eng Perform. 2018. https://doi.org/10.1007/s11665-018-3559-4.

28. Karolczuk A, Carpinteri A, Robak G, Derda S, Prażmowski M. Fatigue failure analysis of three - layer Zr – Ti / Zr – Steel composite plates : an insight into the evolution of cracks initiated at the interfaces. Arch Civil Mech Eng. 2020;20:1–13. https://doi.org/10.1007/s43452-020-00145-8.

29. Xu J, Yang M, Chen D, Ma H, Shen Z, Zhang B, Tian J. Providing a new perspective for obtaining high-quality metal coatings: fabrication and properties studies of TA2 foil on Q235 steel by explosive welding. Arch Civil Mech Eng. 2021. https://doi.org/10.1007/s43452-021-00271-x.

30. Jiang F, Deng ZL, Zhao K, Sun J. Fatigue crack propagation normal to a plasticity mismatched bimaterial interface. Mater Sci Eng, A. 2003;356:258–66. https://doi.org/10.1016/S0921-5093(03)00142-4.

31. Zhou B, Zhou C, Chang L, Yu X, Ye C, Zhang B. Investigation on fatigue crack growth behavior of Zr702/TA2/Q345R explosive welding composite plate with a through-wall crack. Compos Str. 2020. https://doi.org/10.1016/j.compstruct.2019.111845.

32. Ostroushko D, Mazancova E. Chosen properties of sandwich CrNi steel-ti material after explosive cladding, in: 19th International Conference on Metallurgy and Materials, 2010.

33. Wachowski M, Śnieżek L, Szachogłuchowicz I, Kosturek R, Płociński T. Microstructure and fatigue life of Cp-Ti/316L bimetallic joints obtained by means of explosive welding. Bull Polish Acad Sci Techn Sci 2018; 66:925–933. https://doi.org/10.24425/bpas.2018.125940.

34. Wachowski M, Gloc M, Ślęzak T, Płociński T, Kurzydłowski KJ. The Effect of heat treatment on the microstructure and properties of explosively welded titanium-steel plates. J Mater Eng Perform. 2017. https://doi.org/10.1007/s11665-017-2520-2.

35. Kurek A, Wachowski M, Niesłony A, Płociński T, Kurzydłowski KJ. Fatigue tests and metallographic of explosively cladded steel-titanium bimetal. Arch Metall Mater. 2014;59:1566–70. https://doi.org/10.2478/amm-2014-0265.

36. Karolczuk A, Kowalski M, Bański R, Żok F. Fatigue phenomena in explosively welded steel–titanium clad components subjected to push–pull loading. Int J Fatigue. 2013;48:101–8. https://doi.org/10.1016/j.ijfatigue.2012.10.007.

37. Derda S, Karolczuk A, Robak G, Prażmowski M. Analysis of the fatigue life of metal composites with a layer of zirconium alloy. MATEC Web Confer. 2021;338:01004. https://doi.org/10.1051/matecconf/202133801004.

38. Derda S, Karolczuk A, Prażmowski M, Kurek A, Wachowski M, Paul H. Fatigue life and cyclic creep of tantalum / copper/steel layerwise plates under tension loading at room temperature. Int J Fatigue. 2022;162:106977. https://doi.org/10.1016/j.ijfatigue.2022.106977.

39. Szmul M, Stan-Glowinska K, Janusz-Skuza M, Bigos A, Chudzio A, Szulc Z, Wojewoda-Budka J. The interface zone of explosively welded titanium/steel after short-term heat treatment. Metall Mater Trans A Phys Metall Mater Sci. 2021;52:1588–95. https://doi.org/10.1007/s11661-021-06174-z.

40. Rasmussen CE, Williams CKI. Gaussian process for machine learning, The MIT Press, 2006. www.GaussianProcess.org/gpml.

41. Swiler LP, Gulian M, Frankel AL, Safta C, Jakeman JD. A Survey of constrained gaussian process regression: approaches and implementation challenges. J Mach Learn Model Comput. 2020;1:119–56. https://doi.org/10.1615/jmachlearnmodelcomput.2020035155.

42. Chopra OK, Shack WJ. Review of the margins for ASME code fatigue design curve – effects of surface roughness and material variability. Washington. 2003. https://doi.org/10.2172/925073.

43. Karolczuk A, Kluger K, Derda S, Prażmowski M, Paul H. Influence of impact velocity on the residual stress, tensile strength, and structural properties of an explosively welded composite plate. Materials. 2020. https://doi.org/10.3390/ma13122686.

44. Paul H, Morgiel J, Baudin T, Brisset F, Prażmowski M, Miszczyk M. Characterization of explosive weld joints by TEM and SEM/EBSD. Arch Metall Mater. 2014;59:1129–36. https://doi.org/10.2478/amm-2014-0197.

45. Gloc M, Wachowski M, Plocinski T, Kurzydlowski KJ. Microstructural and microanalysis investigations of bond titanium grade1/low alloy steel st52-3N obtained by explosive welding. J Alloys Compd. 2016;671:446–51. https://doi.org/10.1016/j.jallcom.2016.02.120.

46. Prasanthi TN, Sudha C, Saroja S. Explosive cladding and post-weld heat treatment of mild steel and titanium. Mater Des. 2016;93:180–93. https://doi.org/10.1016/j.matdes.2015.12.120.

47. Dodd B, Bai Y. 1 - Introduction, In: Dodd B, Bai Y (Eds.), Adiabatic shear localization (Second Edition), Second Edi, Elsevier, Oxford, 2012: pp. 1–20. https://doi.org/10.1016/B978-0-08-097781-2.00001-0.

48. Karolczuk A, Derda S, Robak G, Prazmowski M. Fatigue test data of corrosion-resistant explosively welded heterostructured plates. Mendeley Data, V1. 2022. https://doi.org/10.17632/mc8bc9tm59.1.

49. Gao J, Wang J, Xu Z, Wang C, Yan S. Multiaxial fatigue prediction and uncertainty quantification based on back propagation neural network and Gaussian process regression. Int J Fatigue. 2023;168:107361. https://doi.org/10.1016/j.ijfatigue.2022.107361.

50. Karolczuk A, Słoński M. Application of the Gaussian process for fatigue life prediction under multiaxial loading. Mech Syst Signal Process. 2022;167:108599. https://doi.org/10.1016/j.ymssp.2021.108599.

51. Greenwell BM, Boehmke BC, McCarthy AJ. A simple and effective model-based variable importance measure 2018;1–27. arXiv:1805.04755v1

52. Goldstein A, Kapelner A, Bleich J, Pitkin E. Peeking inside the black box: visualizing statistical learning with plots of individual conditional expectation. J Comput Graph Stat. 2015;24:44–65. https://doi.org/10.1080/10618600.2014.907095.

53. Pan B, Xie H, Wang Z. Equivalence of digital image correlation criteria for pattern matching. Appl Opt. 2010;49:5501–9. https://doi.org/10.1364/AO.49.005501.

54. Song J, Kostka A, Veehmayer M, Raabe D. Hierarchical microstructure of explosive joints: example of titanium to steel cladding. Mater Sci Eng A. 2011;528:2641–7. https://doi.org/10.1016/j.msea.2010.11.092.

55. Leitner T, Hohenwarter A, Ochensberger W, Pippan R. Fatigue crack growth anisotropy in ultrafine-grained iron. Acta Mater. 2017;126:154–65. https://doi.org/10.1016/j.actamat.2016.12.059.

56. Li C, Wu S, Zhang J, Xie L, Zhang Y. Determination of the fatigue P-S-N curves – A critical review and improved backward statistical inference method. Int J Fatigue. 2020;139:105789. https://doi.org/10.1016/j.ijfatigue.2020.105789.

57. Pang JC, Li SX, Wang ZG, Zhang ZF. Relations between fatigue strength and other mechanical properties of metallic materials. Fatigue Fract Eng Mater Struct. 2014;37:958–76. https://doi.org/10.1111/ffe.12158.

58. Murakami Y, Endo M. Effects of defects, inclusions and inhomogeneities on fatigue strength. Int J Fatigue. 1994;16:163–82. https://doi.org/10.1016/0142-1123(94)90001-9.